CrystEngComm

PAPER

View Article Online
View Journal

Cite this: DOI: 10.1039/d6ce00175k

Thermochromism and X-ray detection capabilities of a hybrid double metal halide perovskite $(C_3H_{12}N_2)_2AgBiBr_8$

Kanika Parashar,[a] Tamanna Pinky,[a] Nobuyuki Yamamoto,[a] S. A. Keishana Navodye,[b] G. T. Kasun Kalhara Gunasooriya,[b] Mark D. Smith[c] and Bayram Saparov*[a]

Two-dimensional (2D) layered hybrid double metal halide perovskites have recently gained significant attention as lead-free and environmentally benign alternatives to lead halide perovskites. In this study, we report the photophysical properties of a 2D Dion–Jacobson (DJ) type hybrid double perovskite, $(C_3H_{12}N_2)_2AgBiBr_8$, which exhibits both reversible thermochromism and promising X-ray radiation detection capabilities. This material shows transition from a low-temperature monoclinic $P2_1/n$ phase to a high-temperature monoclinic $C2/m$ phase at 121.83 °C along with a color change from yellow to bright orange. The phase transition is reversible and both single crystals and bulk powder samples of $(C_3H_{12}N_2)_2AgBiBr_8$ remain stable for more than 30 heating–cooling cycles. Optical property characterization shows that $(C_3H_{12}N_2)_2AgBiBr_8$ is a semiconductor with an indirect band gap of 2.42 eV. The material demonstrates a semiconductor resistivity of 2.8×10^{10} Ω cm, lower than those of other reported DJ-type hybrid double perovskites, and also shows response towards soft X-rays (8 keV) with a detector sensitivity of 188.52 μCGy^{-1} cm^{-2}. These properties along with a very high signal-to-noise ratio (SNR) value (111.45) indicate the potential of $(C_3H_{12}N_2)_2AgBiBr_8$ for direct radiation detection.

Received 4th March 2026,
Accepted 26th May 2026

DOI: 10.1039/d6ce00175k

rsc.li/crystengcomm

Introduction

Over the years, the need for X-ray detection technologies has grown in multiple fields such as medicine, airport security, non-destructive testing and industrial inspections.[1] In the past decade, conventional semiconductor materials like cadmium zinc telluride (CZT), gallium oxide (Ga_2O_3), amorphous selenium (α-Se), high-purity germanium, *etc.* have been widely used for radiation detection. However, certain challenges such as inferior hole charge transport (*e.g.*, in CZT crystals), large leakage currents (*e.g.*, in high-purity germanium), low X-ray absorption (*e.g.*, in α-Se), high manufacturing costs and complex synthesis limit their further commercial applications.[2–4] These drawbacks of currently used materials motivate additional research to develop alternative materials with excellent performance, high X-ray attenuation and low-cost synthesis.

Recently, hybrid organic–inorganic metal halide perovskites have been investigated as potential candidates for radiation detection owing to their simple solution-based synthesis, tunable band gaps, strong X-ray attenuation, and high carrier mobilities.[5–8] Among the explored hybrid metal halide perovskites, most studied materials are three-dimensional (3D) hybrid lead halide perovskites like methylammonium lead iodide ($MAPbI_3$) and formamidinium lead bromide ($FAPbBr_3$) due to their superior detection performance.[9,10] Nevertheless, the risk of lead toxicity and environmental instability of these materials hinder their commercial development.[11] Furthermore, their 3D structural arrangement results in severe ion migration, which impacts the device performance causing low operational stability of X-ray detectors.[12,13] Hence, the search for non-toxic, lead-free alternatives to $APbX_3$ halides with greater operational performance and superior stability is significant.

One proposed solution lies in two-dimensional (2D) hybrid double metal halide perovskites, which have recently been studied as promising alternatives of lead-based materials in certain fields. Double metal halide perovskites are produced by substituting Pb^{2+} with a combination of less-toxic or non-toxic monovalent and trivalent metal cations such as Ag^+, Cu^+, Sb^{3+}, Bi^{3+}, In^{3+}, *etc.*[14,15] Their 2D layered structures can result in low ion migration, better structural stability, and unique anisotropic charge transport characteristics for stable X-ray detectors.[16] In the literature, two often-discussed classes of 2D hybrid double metal halide perovskites are (i) Dion–Jacobson (DJ) $A_2B^IB^{III}X_8$ halides and (ii) Ruddlesden–Popper (RP) phases with the $A_4B^IB^{III}X_8$ structure (where A = organic cation, $B^I = Ag^+, Cu^+, K^+$; $B^{III} = Sb^{3+}, Bi^{3+}, In^{3+}$). In RP-type perovskites, two layers of

---

[a] Department of Chemistry & Biochemistry, The University of Oklahoma, Norman, Oklahoma 73019-5251, USA. E-mail: saparov@ou.edu
[b] School of Sustainable Chemical, Biological and Materials Engineering, The University of Oklahoma, Norman, Oklahoma 73019-5251, USA
[c] Department of Chemistry and Biochemistry, University of South Carolina, Columbia, South Carolina 29208, USA

monovalent A^+ organic cations reside between inorganic layers with a van der Waals gap between them, causing a larger interlayer spacing unfavorable for charge transfer.[17] In contrast, DJ-type perovskites with a monolayer of divalent A^{2+} cations interacting strongly with inorganic slabs *via* hydrogen bonding typically have shorter interlayer distances and stronger lattice stiffness.[18] These features result in enhanced charge separation, lower quantum confinement effects, suppressed ion migration and ultimately could give excellent X-ray detection performance for DJ-type perovskites.[19]

In this work, we report the synthesis, crystal structure, reversible thermochromic behavior and radiation detection properties of a DJ-type 2D hybrid double metal halide perovskite $(C_3H_{12}N_2)_2AgBiBr_8$. This compound has been discussed in a previous report as an efficient photocatalyst for oxidation of toluene,[20] however, the optoelectronic properties and its potential radiation detection applications are still unexplored. The use of propane-1,3-diammonium cation results in the shortest interlayer (~3.86 Å) distance for a 2D perovskite structure as other materials with nearest aliphatic diammonium cations have larger interlayer distances. For example, $(ED)_4AgBiBr_{12}$ (ED = ethylenediammonium cation) (~6.65 Å) and $(BDA)_2AgBiBr_8$ (BDA is 1,4-butanediammonium cation) (~4.5 Å) have larger interlayer distances due to their distinct structural arrangement and longer ammonium-to-ammonium distance, respectively.[20,21] This motivated us to investigate the potential advantages of a DJ perovskite with the shortest interlayer distance for optoelectronic applications.

Beyond its interesting crystal structure, we find that $(C_3H_{12}N_2)_2AgBiBr_8$ exhibits reversible thermochromism due to a structural transition at 121.83 °C, confirmed by Differential Scanning Calorimetry (DSC) and Single Crystal X-ray Diffraction (SCXRD) measurements at low and high temperatures. Hybrid metal halide perovskites with thermochromism are exciting due to their potential in smart temperature coatings, temperature sensors and next-generation anticounterfeiting technologies.[22–24] To date, thermochromism has been reported for single metal halide perovskites such as 2D RP-type $(MBA)_2CuCl_4$ (MBA is 4-methoxybenzylaminium),[25] $(BA)_2CuCl_4$ (BA is benzylaminium),[25] $(C_6H_5C_2H_4NH_3)_2PbBr_4$,[26] 2D DJ-type $(3AMP)PbI_4$ (3AMP is 3-(aminomethyl)pyridinium),[27] *etc.*, with very few studies focused on reversible thermochromism of a 2D DJ-type hybrid double metal halide perovskite. Based on our knowledge, only one example of thermochromic DJ-type hybrid double metal halide perovskite, *i.e.* $(H_2MPP)_2[BiAgI_8]$ (where H_2MPP is 1-methylpiperidinium-4-amine), is reported to date.[28] The photophysical properties of $(C_3H_{12}N_2)_2AgBiBr_8$, and its potential for direct radiation detection, are discussed together with the results of Density Functional Theory (DFT) calculations.

Experimental section

Materials

All chemicals were used as purchased without further purification including silver(I) oxide (99.99% metals basis, Alfa Aesar), bismuth(III) oxide (99.999%, Alfa Aesar), 1,3-diaminopropane (98%, Thermo Scientific), hydrobromic acid (HBr) (48 wt% in water, Sigma Aldrich), and hypophosphorous acid (H_3PO_2) (50%, Sigma Aldrich).

Synthesis of $(C_3H_{12}N_2)_2AgBiBr_8$

$(C_3H_{12}N_2)_2AgBiBr_8$ was synthesized under ambient conditions in a standard fume hood. Stoichiometric amounts of Ag_2O (0.058 g) and Bi_2O_3 (0.1165 g) were dissolved in 1 mL of HBr and 0.15 mL of H_3PO_2 to make a clear solution. Then, 0.083 mL of 1,3-diaminopropane was added dropwise with continuous stirring in an ice-bath. After the addition of 1,3-diaminopropane, the solution was stirred and heated at approximately 120 °C to completely dissolve the reactants. Thereafter, the precursor solution was left on a hot plate at 40 °C for 24 hours resulting in plate-like, yellow-colored crystals of $(C_3H_{12}N_2)_2AgBiBr_8$ with a yield of 97%. The obtained crystals up to (4 × 2 × 1) mm^3 size were stored under a nitrogen-filled glovebox for further characterization.

Powder X-ray Diffraction (PXRD)

Powder X-ray Diffraction (PXRD) measurements were conducted on powder samples of $(C_3H_{12}N_2)_2AgBiBr_8$ by using a Rigaku MiniFlex600 system equipped with a Cu Kα radiation source. The powder sample was prepared by grounding the as-synthesized crystals of $(C_3H_{12}N_2)_2AgBiBr_8$ in ambient air. PXRD scans in the range of 3–90° (2θ) were taken with a step value of 0.02°; the obtained data were analyzed using PDXL2 software.

Single Crystal X-ray Diffraction (SCXRD)

X-ray intensity data from a yellow crystal was collected at 100 K using a Bruker D8 QUEST diffractometer equipped with a PHOTON-II area detector and an Incoatec microfocus source (Mo Kα radiation, λ = 0.71073 Å). The raw area detector data frames were reduced, scaled and corrected for absorption effects using Bruker APEX3, SAINT+ and SADABS programs.[29,30] The structure was solved with SHELXT.[31] Subsequent difference Fourier calculations and full-matrix least-squares refinement against F^2 were performed with SHELXL-2019/3 (ref. 32) using OLEX2.[33]

For high temperature SCXRD measurements, a yellow crystal was heated from room temperature to 400 K at a rate of 100 K h^{-1} prior to the measurements. Measurements were performed on a Bruker D8 QUEST diffractometer equipped with an Incoatec Iμs 2.0 microfocus Mo Kα X-ray source and a PHOTON-II area detector. The frames were integrated with the SAINT V8.41 package using a narrow-frame algorithm.[34] Data were corrected for absorption effects using the Multi-Scan method in SADABS 2016/2. The calculated minimum and maximum transmission coefficients (based on crystal size) are 0.027 and 0.082. The structure was solved with intrinsic-methods and refined with full-matrix-least squares using the SHELX suite of programs in Olex2.[31–33] Table S1 consists of detailed information about the data collection and crystallographic parameters for $(C_3H_{12}N_2)_2AgBiBr_8$ at both 100 K and 400 K. The atomic coordinates, equivalent isotropic displacement parameters, bond angles and selected interatomic distances for $(C_3H_{12}N_2)_2AgBiBr_8$ at 100 K and 400 K are given in Tables S2–S5. The crystallographic information file (CIF) for $(C_3H_{12}N_2)_2AgBiBr_8$ has been submitted to the Cambridge Crystallographic Data Centre (CCDC) database under deposition numbers 2532216 and 2532217.

Thermogravimetric Analysis (TGA) and Differential Scanning Calorimetry (DSC)

Simultaneous TGA and DSC measurements were performed on approximately 10 mg polycrystalline samples of $(C_3H_{12}N_2)_2AgBiBr_8$ using a TA Instruments SDT 650 thermal analyzer system. The measurements were performed in the 25 °C to 475 °C range at a heating rate of 5 °C min^{-1} under a continuous flow of nitrogen gas at a flow rate of 100 mL min^{-1}.

The melting transition obtained from the DSC plot was further confirmed *via* a Mel-Temp melting point apparatus (200 W, 110–120 V, 50/60 Hz; laboratory devices, Cambridge, MA, USA). The measurement was performed on a powder sample (∼2 mg) of $(C_3H_{12}N_2)_2AgBiBr_8$ in a temperature range of 25 °C to 320 °C.

UV-vis spectroscopy

UV-vis diffuse reflectance measurements were performed on a finely ground powder sample of $(C_3H_{12}N_2)_2AgBiBr_8$ using a PerkinElmer Lambda 750 UV-vis-NIR spectrometer equipped with a 100 mm Spectralon InGaAs integrating sphere, covering a range of 250–1100 nm. The collected diffuse reflectance data were converted into pseudo-absorption spectra using the Kubelka–Munk function $F(R) = \alpha/S = (1 - R)^2/2R$, where α is the absorption coefficient, S denotes the scattering coefficient and R represents the reflectance.

Density Functional Theory (DFT) calculations

Periodic spin-polarized density functional theory (DFT) structure optimizations were performed using the Perdew–Burke–Ernzerhof (PBE)[35] exchange correlational functional with D3 dispersion corrections, a plane-wave basis set with a cut-off kinetic energy of 500 eV for all the bulk structures, and the projector-augmented wave (PAW) method as implemented in the Vienna *Ab initio* Simulation Package (VASP version 6.4.3).[36,37] The electronic convergence criterion was 10^{-6} eV, while the force criterion for geometry relaxation was 0.01 eV $Å^{-1}$. To obtain numerically converged results, the Brillouin zone of the unit cell was sampled with a 2 × 2 × 1 Γ-centered k-point grid. The band structure analysis was carried out using the Python Materials Genomics (Pymatgen) package.[38]

Electrical characterization and X-ray response measurements

A freshly prepared single crystal of $(C_3H_{12}N_2)_2AgBiBr_8$ was selected for performing electrical characterization and X-ray response measurements. Two opposite sides of the selected crystal were brushed with a high-quality silver paste purchased from Ted Pella, Inc. A Keithley 6487 pico-ammeter was used for performing electrical measurements including current–voltage (*I–V*) and space-charge-limited-current (SCLC) measurements. For both *I–V* and SCLC measurements, the voltage scan was carried out with a step size of 2 V. The X-ray response measurements were conducted by exposing a fabricated prototype single crystal-based detector to 8 keV soft X-rays produced from a Rigaku Micromax 007HF microfocus X-ray generator equipped with a Cu target. For careful calibration of X-ray radiation dose rate, a commercial dosimeter was used.

Results and discussion

High-quality single crystals of $(C_3H_{12}N_2)_2AgBiBr_8$ were synthesized by using a facile slow evaporation method [Fig. S1]. Well-matched room temperature powder X-ray diffraction (PXRD) patterns of the as-synthesized crystals and single crystal X-ray diffraction (SCXRD) data confirmed the phase purity and crystallinity of the sample [Fig. S2(a) and (b)]. The ease of synthesizing good quality and large crystals are important advantages of optoelectronic metal halides for their prospective practical applications.

SCXRD data acquired at 100 K confirms that $(C_3H_{12}N_2)_2AgBiBr_8$ crystallizes in a monoclinic crystal system with a space group of $P2_1/n$. Fig. 1(a) and S3 depict a two-dimensional (2D) DJ-type layered structure of $(C_3H_{12}N_2)_2AgBiBr_8$ with alternating organic and inorganic layers stacked along the c-axis. The inorganic layer consists of alternating $[AgBr_6]^{5-}$ and $[BiBr_6]^{3-}$ octahedra that share common corners along the ab-plane to form the $[AgBiBr_8]^{4-}$ layers; the inorganic anionic layers are separated by a monolayer of $[C_3H_{12}N_2]^{2+}$ cations maintaining the overall charge neutrality [Fig. 1(a) and (b)]. A strong and extensive network of NH⋯Br hydrogen bonds between $[C_3H_{12}N_2]^{2+}$ organic cations and inorganic layers stabilize the overall structure [see Fig. S4]. Within the $[AgBr_6]^{5-}$ and $[BiBr_6]^{3-}$ polyhedra, the Ag–Br bond distances range from 2.619(6) Å to 3.037(5) Å whereas the Bi–Br bond distances lie in the range of 2.832(5) Å to 2.856(6) Å [Fig. 2(a) and (b) and S5], which are evidences of the distortions in the $[AgBiBr_8]^{4-}$ layers. This is further evidenced by the bridging angles as low as Bi1–Br4–Ag1 = 151.29(2)° [Table S4]. Such distortions are expected due to the difference in the sizes of the monovalent and trivalent metal cations in double metal halide perovskites. Indeed, distortions of inorganic halide octahedra and octahedral tilting within the in-plane direction of inorganic layers is commonly found in other reported DJ-type double metal halide perovskites such as $(4\text{-AP})_2AgBiBr_8$ (4-AP is 4-aminopyridine), $(HA)_2AgBiBr_8$ (HA is histammonium) and $(4N4)_2AgBiBr_8$ (4N4 is $NH_3C_4H_8NH_3$).[17,19,39]

Upon closer examination, it was observed that the organic cation penetration depth in the inorganic layers is about 1.493 Å, which reduces the interlayer spacing (*i.e.*, Br–Br distances on the adjacent layers) to 3.86 Å [Fig. S6]. This interlayer Br–Br distances are comparatively shorter than other reported DJ-type halide

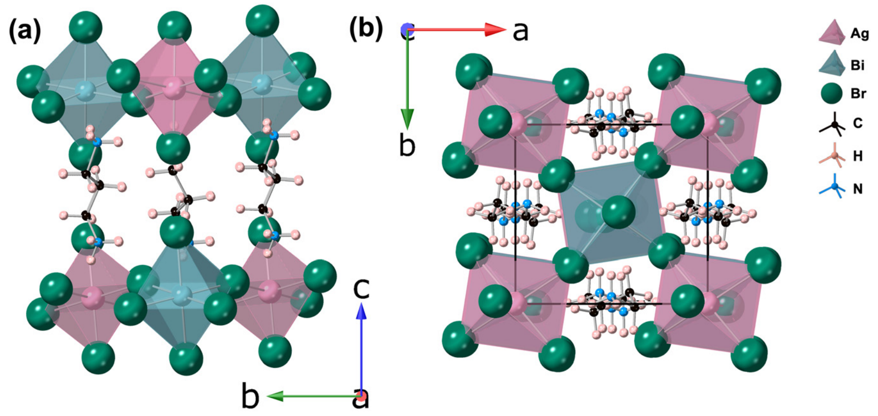

Fig. 1 Crystal structure of $(C_3H_{12}N_2)_2AgBiBr_8$ viewed down the (a) *a*- and (b) *c*-axes. Silver, bismuth, bromine, nitrogen, carbon and hydrogen are shown by pink, bluish-green, green, blue, black and peach spheres, respectively.

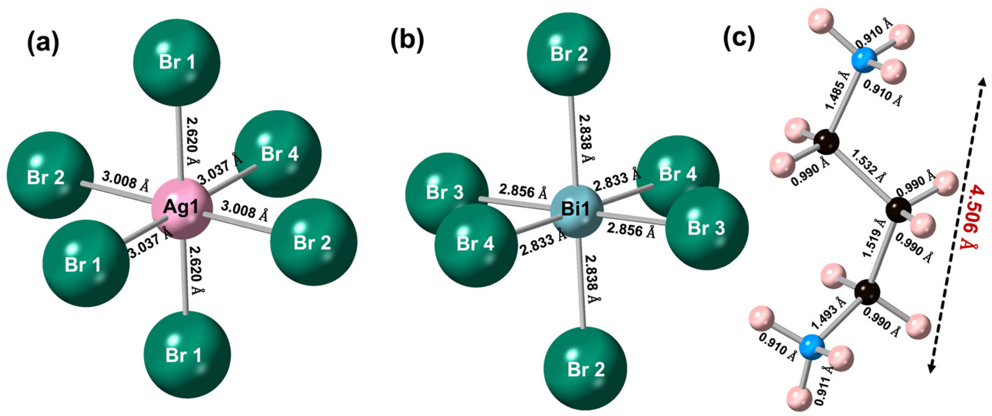

Fig. 2 Interatomic distances in the coordination environments of (a) silver and (b) bismuth, and (c) in the organic $C_3H_{12}N_2^{2+}$ cation. Silver, bismuth, bromine, nitrogen, carbon and hydrogen are represented by pink, bluish-green, green, blue, black and peach spheres, respectively.

perovskites such as (*m*-PDA)$MA_{n-1}Pb_nI_{3n+1}$ (n = 2 and 3) (*m*-PDA is *m*-phenylenediammonium and MA is methylammonium) (4.00 to 4.04 Å) and $(HIS)_2AgSbBr_8$ (HIS is histammonium) (~4.00 Å).[40,41] A shorter interlayer spacing results in the reduced quantum confinement effect and energy barrier for charge transfer between the inorganic layers. This results in better charge separation and carrier transfer, beneficial for superior radiation response.[17]

To examine the thermal stability of $(C_3H_{12}N_2)_2AgBiBr_8$, parallel thermogravimetric analysis (TGA) and differential scanning calorimetry (DSC) measurements were performed on a polycrystalline sample [Fig. 3]. The TGA results reveal high thermal stability of $(C_3H_{12}N_2)_2AgBiBr_8$ as no noticeable weight loss was observed up to 300 °C. Above 300 °C, the sample starts evaporating and decomposes with continuous weight loss up to 450 °C. DSC curves, recorded from room temperature to 450 °C, showed three different endothermic features at temperatures 121.83 °C, 233.90 °C and 327.81 °C. The endothermic feature observed at 233.90 °C corresponds to the melting point of $(C_3H_{12}N_2)_2AgBiBr_8$ as confirmed by observing the crystals melting on the melting point checking apparatus near this temperature. The feature at 327.81 °C relates to the thermal decomposition of $(C_3H_{12}N_2)_2AgBiBr_8$, which is accompanied by the significant weight loss of 75.86%.

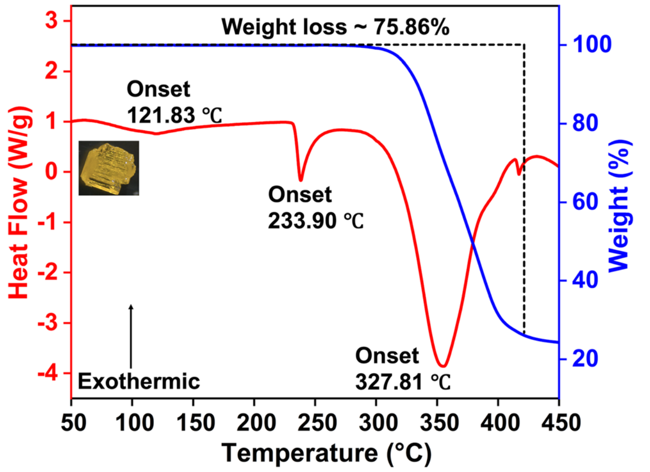

Fig. 3 Thermogravimetric Analysis (TGA, in blue) and Differential Scanning Calorimetry (DSC, in red) curves for $(C_3H_{12}N_2)_2AgBiBr_8$.

The DSC feature at 121.83 °C coincides with the reversible thermochromism observed for $(C_3H_{12}N_2)_2AgBiBr_8$ [see Video S1]. Upon heating, $(C_3H_{12}N_2)_2AgBiBr_8$ single crystals show a dynamic color change from yellow to orange [see Fig. S7(a)], which intensifies with further heating up to ∼240 °C where the crystals start melting. Notably, the crystal color reverts back to its original appearance within few seconds when cooled to room temperature [Video S2]. The temperature dependent color change was also observed in the case of bulk powders of $(C_3H_{12}N_2)_2AgBiBr_8$ [as shown in Fig. S7(b)]. This reversibility was further confirmed through multiple heating–cooling cycles and the $(C_3H_{12}N_2)_2AgBiBr_8$ single crystals exhibit excellent stability during thermal cycling up to more than 30 cycles. This remarkable reversible thermochromism and excellent material stability make $(C_3H_{12}N_2)_2AgBiBr_8$ a candidate material for temperature sensing applications.

In hybrid metal halide perovskites, thermochromic behavior is usually attributed to either complete structural phase transitions or local structural changes like modulation of interatomic distances.[42] To investigate the origin of thermochromic behavior displayed by $(C_3H_{12}N_2)_2AgBiBr_8$, DSC curves were recorded from 30 °C to 200 °C [Fig. S7(c)]. The reversible endothermic/exothermic features at 121.83 °C and 116.29 °C suggest a high-temperature reversible structural phase transition for $(C_3H_{12}N_2)_2AgBiBr_8$. This observation was confirmed by SCXRD measurements performed below (100 K) and above (400 K) the transition temperature. At 100 K, $(C_3H_{12}N_2)_2AgBiBr_8$ crystallizes in the monoclinic space group of $P2_1/n$ with the unit cell dimensions of a = 8.3736(3) Å, b = 7.6960(3) Å, c = 18.2768(7) Å and β = 99.008(1)°. Upon heating above the transition temperature, the structure changes to the monoclinic space group of $C2/m$ with the lattice parameters of a = 18.999(15) Å, b = 7.8787(7) Å, c = 8.3765(8) Å and β = 107.287(3)° [see Fig. S8 and Table S1].

In hybrid metal halide perovskites, the motion of organic cations is greatly dependent on the temperature, which often results in phase transitions.[43] These phase transitions are usually associated with the organic cations' rotation, hydrogen bonding interactions, and the subsequent distortions of the inorganic framework.[44] In $(C_3H_{12}N_2)_2AgBiBr_8$, above the transition temperature (400 K), the $[C_3H_{12}N_2]^{2+}$ organic cations exhibit a dual orientation that result in the formation of mirror-symmetry in the high-temperature phase (HT phase, monoclinic, $C2/m$) [see Fig. S8]. The $[BiBr_6]^{3-}$ and $[AgBr_6]^{5-}$ octahedra show bond distances ranging from 2.8204(5) Å to 2.8502(8) Å and 2.6101(8) Å to 3.008(6) Å, respectively at 400 K [Fig. S9(a) and (b)]. The organic cation also displays visible changes in its bond lengths and ammonium-to-ammonium distance at a higher temperature [Fig. S9(c)]. Interestingly, both $[BiBr_6]^{3-}$ and $[AgBr_6]^{5-}$ show less octahedral tilting with a bridging Bi1–Br4–Ag1 inclination angle of 161.20(3)° (closer to 180°) at a higher temperature [Table S5 and Fig. S10]. Before the phase transition, the inorganic framework of $(C_3H_{12}N_2)_2AgBiBr_8$ displays more distortion and deformation, whereas, after the phase transition, octahedra become more regular with reduced tilting and distortion in the monoclinic $C2/m$ phase.[45] This reduced octahedral tilting and deformation in inorganic layers may arise from hydrogen-bonding rearrangement between organic cations and inorganic layers caused by dynamic motion of organic cations at a higher temperature.[46] The observed increases in the interatomic distances result in the thermal expansion of the unit cell volume from 1163.29(8) $Å^3$ to 1197.27(18) $Å^3$ for $(C_3H_{12}N_2)_2AgBiBr_8$, in line with the temperature-dependent structural changes observed for other hybrid metal halides.[47]

To gain better understanding of the optical properties, diffuse reflectance measurements were performed on polycrystalline powder samples of $(C_3H_{12}N_2)_2AgBiBr_8$. The measurements suggest a sharply defined absorption onset at 2.5 eV [Fig. 4(a)]. The Tauc plots obtained from the diffuse reflectance data, assuming direct and indirect optical transitions for $(C_3H_{12}N_2)_2AgBiBr_8$, give band gap values of 2.62 eV and 2.42 eV, respectively [Fig. 4(b) and (c)]. These values match well with the band gap values of other reported DJ-type hybrid double metal halide perovskites.[19,21]

To evaluate the band edge positions relative to the Fermi level, electronic band structure of $(C_3H_{12}N_2)_2AgBiBr_8$ was calculated using the DFT methods. The valence band maximum (VBM) is located at the gamma (Γ) point, whereas the conduction band minimum (CBM) is at the center point of X and H1, yielding an indirect band gap value of 2.45 eV. This agrees well with the experimentally determined value of 2.42 eV for $(C_3H_{12}N_2)_2AgBiBr_8$ [Fig. 5(a)].

The CBM for $(C_3H_{12}N_2)_2AgBiBr_8$ lies at 2.22 eV whereas the VBM lies at −0.23 eV relative to the Fermi level of the material. The calculated projected density of states (PDOS) plot [Fig. 5(b)] shows that the DOS of the organic part is weak near both VBM and CBM, unlike the DOS from the inorganic component. Therefore, the primary contributions to the frontier states originate from the inorganic component of $(C_3H_{12}N_2)_2AgBiBr_8$. A detailed analysis of the orbital contributions to the PDOS reveals that the VBM of $(C_3H_{12}N_2)_2AgBiBr_8$ is primarily composed of Ag-d and Br-p orbitals whereas the band structure near the CBM contains both Bi-p and Br-p orbitals in $(C_3H_{12}N_2)_2AgBiBr_8$ [Fig. 5(b)]. This observation suggests that the VBM is localized on $[AgBr_6]^{5-}$ anions while CBM lies in $[BiBr_6]^{3-}$ anions, which further supports the observed indirect band gap for $(C_3H_{12}N_2)_2AgBiBr_8$.[48]

Layered 2D DJ hybrid double metal halide perovskites are promising candidates for direct X-ray detection. In the literature, it is suggested that their shorter interlayer distances and higher lattice rigidity make them better at radiation detection compared to the more common RP-type hybrid double metal halide perovskites.[19,49] Despite their advantages, these materials are less explored than the RP phase for ionizing radiation detection applications. Therefore, we investigated the potential of the $(C_3H_{12}N_2)_2AgBiBr_8$ semiconductor for direct X-ray detection by using a fabricated prototype detector based on a single crystal of $(C_3H_{12}N_2)_2AgBiBr_8$ [shown in Fig. S11]. The photon attenuation capability of $(C_3H_{12}N_2)_2AgBiBr_8$ was compared with the commercial X-ray detector material cadmium

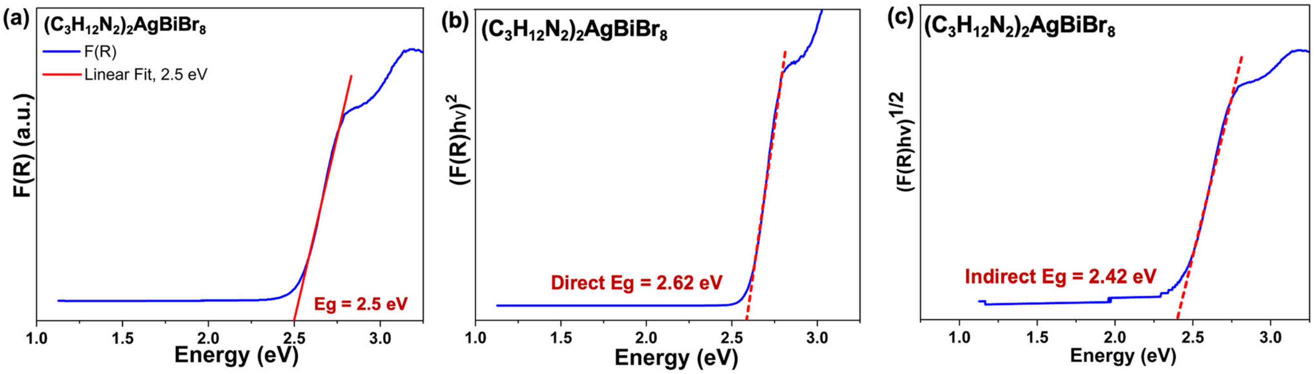

Fig. 4 (a) Diffuse reflectance data for $(C_3H_{12}N_2)_2AgBiBr_8$ plotted as the Kubelka–Munk function, denoted as *F*(*R*). Tauc plots assuming (b) direct and (c) indirect band gaps, respectively.

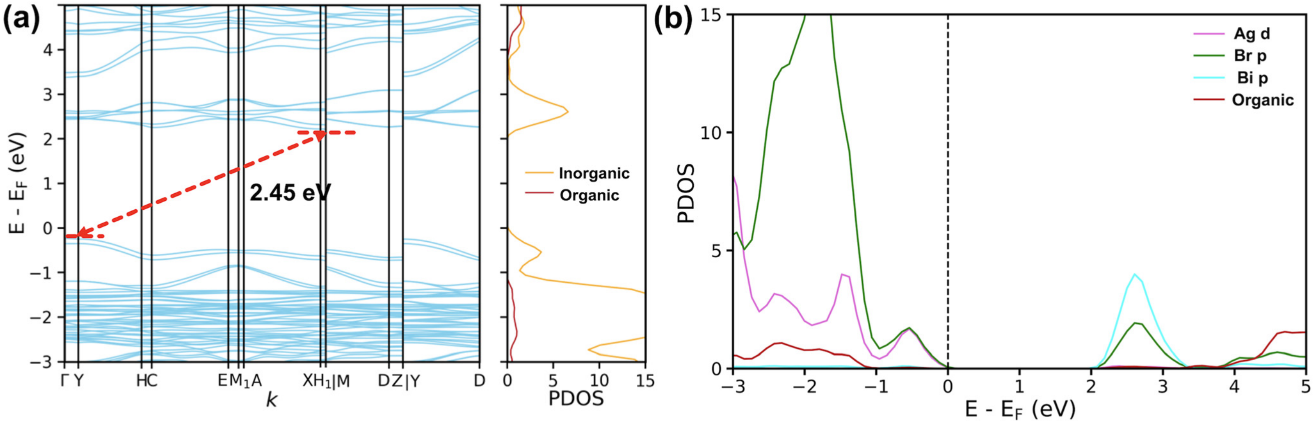

Fig. 5 (a) Electronic band structure plot with a side panel illustrating the projected contributions of organic (C, H and N elements) and inorganic (Ag, Bi and Br elements) states. (b) Projected density of states (PDOS) plot showing the orbital contributions of the inorganic elements in $(C_3H_{12}N_2)_2AgBiBr_8$.

telluride (CdTe), elemental semiconductor silicon (Si) and its RP-type analog $(PA)_4AgBiBr_8$ (PA is *n*-propylammonium cation) for soft low-energy X-rays and high-energy gamma-rays. The comparison shows better photon attenuation ability of $(C_3H_{12}N_2)_2AgBiBr_8$ than $(PA)_4AgBiBr_8$ [Fig. S12] due to the increased average *Z*.

Current–voltage (*I*–*V*) measurements were performed on the $(C_3H_{12}N_2)_2AgBiBr_8$ single crystals. The measured resistivity value is 2.8×10^{10} Ω cm along the *c*-axis (*i.e.*, perpendicular to the layer propagation direction) [see Fig. 6(a) and S13(a)]. This value is close to the resistivity values of some other reported 2D DJ-type hybrid double metal halide perovskites such as $(4\text{-AP})_2AgBiBr_8$ (4-AP is 4-amidinopyridine) (1.7×10^{11} Ω cm),[17] $(HA)_2AgBiBr_8$ (HA^{2+} is histammonium) (8.03×10^{10} Ω cm),[19] and $(HIS)_2AgSbBr_8$ (HIS^{2+} is histammonium) (2.2×10^{11} Ω cm)[41] which are explored for X-ray detection.

To determine the defect trap levels (n_{trap}) of $(C_3H_{12}N_2)_2AgBiBr_8$, we performed space-charge-limited-current (SCLC) measurements. As it can be seen in Fig. 6(b), the SCLC curve shows three different current transition regimes *i.e.*, ohmic (where $I \propto V$), Child (where $I \propto V^2$) and trap-filled limited (TFL) (where $I \propto V^n$, $n > 2$). Here, the TFL regime is attributed to the completely filled defect trap levels with charge carriers inserted through the metal contacts, and therefore, the following formula using the onset voltage of the TFL regime (*i.e.*, $V_{\text{TFL}} = 112$ V) can be utilized to estimate the density of trap levels (n_{trap}):[50]

$$n_{\text{trap}} = \frac{2\varepsilon\varepsilon_0}{eL^2} V_{\text{TFL}}$$

Here, ε is the dielectric constant (=20.32), ε_0 is the vacuum permittivity, and *e* and *L* are the electronic charge and crystal thickness (*i.e.*, 1 mm), respectively. The estimated n_{trap} value is 2.5×10^{11} cm^{-3}, which is much lower than that of the inorganic semiconductors commercially utilized for radiation detection, *e.g.* CdTe ($\sim 4.0 \times 10^{14}$ cm^{-3}),[51] silicon (10^{13} to 10^{14} cm^{-3}),[52] and the RP-type hybrid double metal halide perovskite $(PA)_4AgBiBr_8$ (7.90×10^{11} cm^{-3}) all have higher n_{trap} values.[21]

To further test the potential of $(C_3H_{12}N_2)_2AgBiBr_8$ for X-ray detection, a prototype X-ray detector was fabricated and exposed to soft 8 keV X-rays. The X-ray on/off measurements

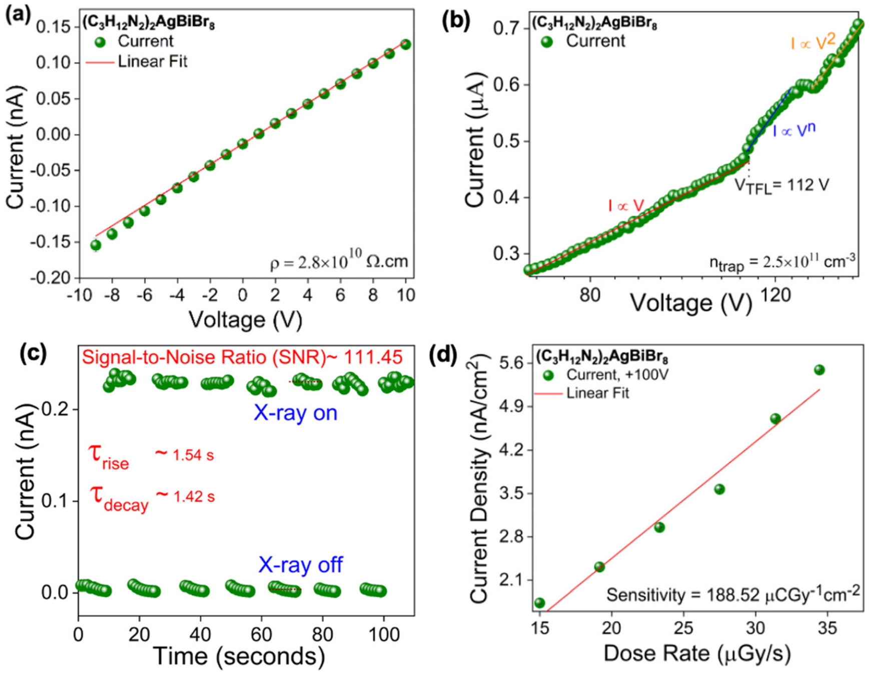

Fig. 6 (a) Current–voltage (*I–V*) measurement results for $(C_3H_{12}N_2)_2AgBiBr_8$. (b) Space-charge-limited-current (SCLC) curve to measure defect trap levels (n_{trap}) in $(C_3H_{12}N_2)_2AgBiBr_8$ single crystals. (c) X-ray on/off current response measurements and (d) X-ray detection sensitivity plot for $(C_3H_{12}N_2)_2AgBiBr_8$.

were performed for $(C_3H_{12}N_2)_2AgBiBr_8$ single crystals, suggesting a remarkably high signal-to-noise ratio (SNR) of 111.45 (here SNR = $I_{\mathrm{On}} - I_{\mathrm{Off}}/I_{\mathrm{Off}}$) and its excellent response towards soft X-rays. To the best of our knowledge, this SNR value is the highest among all the reported 2D DJ type hybrid double metal halide perovskites to date, indicating the outstanding capability of $(C_3H_{12}N_2)_2AgBiBr_8$ at generating high-resolution and high-quality X-ray images beneficial for practical applications [Fig. 6(c)].[53,54] These promising performance metrics are attributed to the very short interlayer distances in $(C_3H_{12}N_2)_2AgBiBr_8$. Furthermore, the X-ray induced current rise time (τ_{rise}, ~1.54 s) and decay time (τ_{decay}, ~1.42 s) were calculated using the 10% to 90% of current amplitude. Following this, we determined the detector sensitivity for $(C_3H_{12}N_2)_2AgBiBr_8$, which is another important performance measure for X-ray detection applications. The sensitivity value is measured to be 188.52 $\mu CGy^{-1}\ cm^{-2}$ (E = 100 V mm^{-1}), which is far superior to the RP-type $(PA)_4AgBiBr_8$ (6.89 $\mu CGy^{-1}\ cm^{-2}$ (at 40 V bias)) [Fig. 6(d)].[55] In order to investigate the long-term detector operational stability under continuous X-ray irradiation, the prototype detector was continuously exposed to the 8 keV X-rays generated from the X-ray generator equipped with a Cu target. Expectedly, an initial drift was observed in the X-ray induced current within the 9 minutes of measurement time attributed to ion migration as normally observed for perovskite-based semiconductors [Fig. S13(b)].[4,56,57] With extended exposure, the material showed unstable current response with a visible drop in the X-ray generated current, similar to other reported perovskite-based X-ray detectors.[58]

Conclusions

In conclusion, this work focusses on the characterization of a 2D Dion–Jacobson (DJ) type hybrid double metal halide perovskite $(C_3H_{12}N_2)_2AgBiBr_8$ with promising semiconductor properties for X-ray detection applications. The material undergoes a reversible structural phase transition from its low-temperature phase (monoclinic, $P2_1/n$) to a high-temperature phase (monoclinic, $C2/m$) at 121.83 °C. This phase transition is accompanied by a change of color from yellow (LT phase) to bright-orange (HT phase). The material remains stable when temperature is cycled through this reversible thermochromic transition. Diffuse reflectance measurements and Tauc plot analysis suggest an indirect band gap of 2.42 eV for $(C_3H_{12}N_2)_2AgBiBr_8$, further confirmed by DFT calculations.

$(C_3H_{12}N_2)_2AgBiBr_8$ shows a semiconductor resistivity of 2.8 × 10^{10} Ω cm, lower than values reported for other reported DJ-type hybrid double metal halide perovskites such as $(4\text{-}AP)_2AgBiBr_8$ (1.7 × 10^{11} Ω cm), $(HIS)_2AgSbBr_8$ (2.2 × 10^{11} Ω cm), and $(HA)_2AgBiBr_8$ (8.03 × 10^{10} Ω cm), maintaining a better balance between the charge carrier transport and leakage current. Measurements done by using a fabricated prototype X-ray detector displayed excellent X-ray response and detector sensitivity of 188.52 $\mu CGy^{-1}\ cm^{-2}$ (100 V mm^{-1}) which is better than the closest Ruddlesden–Popper (RP) type analog $(PA)_4AgBiBr_8$ (6.89 $\mu CGy^{-1}\ cm^{-2}$ (at 40 V bias)),[55] and comparable to other DJ-type hybrid double metal halide perovskites *i.e.*, $(HIS)_2AgSbBr_8$ (223 $\mu CGy^{-1}\ cm^{-2}$), and $(HA)_2AgBiBr_8$ (252.38 $\mu CGy^{-1}\ cm^{-2}$). This observation is supportive of the judgment that DJ-type perovskites with reduced interlayer distances may be more promising for radiation detection compared to their RP counterparts. Furthermore, the signal-to-noise (SNR) ratio value of 111.45 for $(C_3H_{12}N_2)_2AgBiBr_8$ surpasses SNRs of prior reported DJ-type double metal halide perovskites suggesting the material's superior ability of generating high-quality images for real-time X-ray detection applications. Overall, this study highlights the promising X-ray radiation detection properties of 2D DJ-type hybrid double perovskites with stability issues remaining a challenge.

Author contributions

Kanika Parashar: methodology, investigation, formal analysis, visualization, and software, validation, writing – original draft, writing – review & editing. Tamanna Pinky: methodology, investigation, data curation, writing – review & editing. Nobuyuki Yamamoto: formal analysis, data curation, software, resources, and writing – original draft. S. A. Keishana Navodye: software, formal analysis, resources, writing – review & editing. G. T. Kasun Kalhara Gunasooriya: investigation, software, resources, writing – review & editing. Mark D. Smith: investigation, formal analysis, software, data curation, and supervision. Bayram Saparov: conceptualization, resources, writing – original draft, writing – review & editing, supervision, and funding acquisition.

Conflicts of interest

There are no conflicts to declare.

Data availability

The data supporting this article have been provided as supplementary information (SI).

Supplementary information: selected single crystal data, structure refinement parameters, atomic coordinates, equivalent isotropic displacement parameters, bond angles and selected interatomic distances for $(C_3H_{12}N_2)_2AgBiBr_8$ at 100 K and 400 K, photographs of single crystals of $(C_3H_{12}N_2)_2AgBiBr_8$, simulated diffraction data comparison with room-temperature PXRD for $(C_3H_{12}N_2)_2AgBiBr_8$, single crystal structure of $(C_3H_{12}N_2)_2AgBiBr_8$, H-bonding network of $[AgBiBr_8]^{4-}$ inorganic layers with surrounding $[C_3H_{12}N_2]^{2+}$ organic cations, distortions in inorganic layers of $(C_3H_{12}N_2)_2AgBiBr_8$ at 100 K and 400 K, interlayer spacing and penetration depth of organic cations, photographs of single crystals, bulk powders and TGA/DSC curves of $(C_3H_{12}N_2)_2AgBiBr_8$ under heating-cooling cycles, crystal structures of $(C_3H_{12}N_2)_2AgBiBr_8$ at 100 K and 400 K, coordination environments of silver, bismuth, and $[C_3H_{12}N_2]^{2+}$ organic cations at 100 K and 400 K, set-up used for electrical measurements and schematic diagram of fabricated prototype detector used for X-ray response measurements, photon attenuation comparison plot, an indexed room-temperature PXRD pattern of $(C_3H_{12}N_2)_2AgBiBr_8$ single crystal, operational stability test results under continuous X-ray exposure, and videos S1 and S2 showing reversible thermochromic behavior of $(C_3H_{12}N_2)_2AgBiBr_8$ single crystals (mp4). Crystallographic data for $(C_3H_{12}N_2)_2AgBiBr_8$ at 100 K and 400 K has been deposited at CCDC under 2532216 and 2532217. See DOI: https://doi.org/10.1039/d6ce00175k.

CCDC 2532216 and 2532217 contain the supplementary crystallographic data for this paper.[59a,b] Moreover, the optimized DFT structures and data can be accessed using the link https://github.com/gunasooriya-lab/manuscripts.

Acknowledgements

This work received support from the U.S. Department of Energy under award no. DE-SC0021158. We gratefully acknowledge the support for the acquisition of the Bruker D8 QUEST diffractometer from the NSF MRI program (CHE-1726630). We are sincerely thankful to Dr. Leonard Thomas and Dr. Zheng Zhang for their kind help with the X-ray response measurements. To perform X-ray response measurements, the Biomolecular Structure Core (BSC)-Norman facility was used. The BSC-Norman facility is partially supported by the Institutional Development Award (IDeA) from the National Institute of General Medical Sciences of the National Institutes of Health (award P20GM103640 and award P30GM145423), the National Science Foundation (award 0922269), and the University of Oklahoma Department of Chemistry and Biochemistry. Computing for this project was performed at the OU Supercomputing Center for Education & Research (OSCER) at the University of Oklahoma. G. T. K. K. G. gratefully acknowledges start-up funding support from the School of Sustainable Chemical, Biological and Materials Engineering.

References

1 Y. He, I. Hadar and M. G. Kanatzidis, *Nat. Photonics*, 2022, **16**, 14–26.

2 Y. Wang, H. Lou, C.-Y. Yue and X.-W. Lei, *CrystEngComm*, 2022, **24**, 2201–2212.

3 X. He, Y. Deng, D. Ouyang, N. Zhang, J. Wang, A. A. Murthy, I. Spanopoulos, S. M. Islam, Q. Tu and G. Xing, *Chem. Rev.*, 2023, **123**, 1207–1261.

4 Z. Zhang, T. M. Pugliano, D. Cao, D. Kim, R. S. Annam, D. A. Popy, T. Pinky, G. Yang, J. Garg and M. F. Borunda, *J. Mater. Chem. C*, 2023, **11**, 15357–15365.

5 M. Sytnyk, S. Deumel, S. F. Tedde, G. J. Matt and W. Heiss, *Appl. Phys. Lett.*, 2019, **115**, 190501.

6 G. Zheng, H. Wu, Z. Dong, T. Jin, J. Pang, Y. Liu, Z. Zheng, G. Niu, L. Xu and J. Tang, *J. Mater. Chem. C*, 2024, **12**, 6288–6296.

7 Z. Zhang, K. Parashar, A. Roseborough, M. Nyman and B. Saparov, *Eur. J. Inorg. Chem.*, 2025, **28**, e202500156.

8 K. Parashar, Z. Zhang, V. Buturlim, J. Jiang, A. Roseborough, M. Nyman, K. Gofryk, R. Pachter and B. Saparov, *J. Mater. Chem. C*, 2024, **12**, 9372–9384.

9 B. Náfrádi, G. Náfrádi, L. Forró and E. Horváth, *J. Phys. Chem. C*, 2015, **119**, 25204–25208.

10 X. Liu, M. Xu, Y. Hao, J. Fu, F. Wang, B. Zhang, S. Bennett, P. Sellin, W. Jie and Y. Xu, *ACS Appl. Mater. Interfaces*, 2021, **13**, 15383–15390.

11 M. M. Byranvand, W. Zuo, R. Imani, M. Pazoki and M. Saliba, *Chem. Sci.*, 2022, **13**, 6766–6781.

12 Y. Li, Y. Lei, H. Wang and Z. Jin, *Nano-Micro Lett.*, 2023, **15**, 128.

13 Y. Li, S. Li, D. Chen, C. A. Kocoj, A. Yang, B. T. Diroll and P. Guo, *Sci. Adv.*, 2024, **10**, eadk2778.

14 M. Ghasemi, M. Hao, M. Xiao, P. Chen, D. He, Y. Zhang, W. Chen, J. Fan, J. H. Yun and B. Jia, *Nanophotonics*, 2021, **10**, 2181–2219.

15 L. Mao, S. M. Teicher, C. C. Stoumpos, R. M. Kennard, R. A. DeCrescent, G. Wu, J. A. Schuller, M. L. Chabinyc, A. K. Cheetham and R. Seshadri, *J. Am. Chem. Soc.*, 2019, **141**, 19099–19109.

16 M. Han, Y. Xiao, C. Zhou, Y. Yang, X. Wu, Q. Hu, X. Jin, W. Zhang, J.-S. Hu and Y. Jiang, *Mater. Futures*, 2023, **2**, 012104.

17 G. Chen, H. Dai, Z. K. Zhu, J. Wu, P. Yu, Y. Zeng, Y. Zheng, L. Xu and J. Luo, *Small*, 2024, **20**, 2312281.

18 A. Yadav and S. Ahmad, *ACS Appl. Mater. Interfaces*, 2024, **16**, 43134–43155.

19 Y. Zhou, L. Huang, M. Wu, F. Kuang, K. An, P. Feng, P. He, Y. Pu, J. a. Lai and X. Tang, *J. Mater. Chem. C*, 2024, **12**, 18048–18057.

20 Z.-J. Bai, J. Xiong, Y. Mao, S. Tian, B.-H. Wang, B. Hu, X. Wang, W. Zhou, C.-T. Au and L. Chen, *Cell Rep. Phys. Sci.*, 2023, **4**, 101591.

21 H. Chen, Z. Li, S. Wang, G. Peng, W. Lan, H. Wang and Z. Jin, *Adv. Mater.*, 2024, **36**, 2308872.

22 M. De Bastiani, M. I. Saidaminov, I. Dursun, L. Sinatra, W. Peng, U. Buttner, O. F. Mohammed and O. M. Bakr, *Chem. Mater.*, 2017, **29**, 3367–3370.

23 M. Wan, H.-R. Chen, Y.-N. Wang, K. Shi, J.-Y. Liu, Z.-M. Li, S.-Y. Ye, J.-Y. Li and L.-Z. Chen, *Mater. Chem. Front.*, 2022, **6**, 3094–3101.

24 J. Li, Z.-X. Zhang, T. Zhang, P.-Z. Huang, T. Shao, Y. Zhang and D.-W. Fu, *J. Phys. Chem. C*, 2022, **126**, 16437–16446.

25 G. Teri, Q.-Q. Jia, Q.-F. Luo, H.-F. Ni, D.-W. Fu and Q. Guo, *J. Mater. Chem. C*, 2023, **11**, 8903–8907.

26 X. Song, X. Liu, D. Zhang, J. Liao, S. Zhu and W. Zheng, *J. Am. Chem. Soc.*, 2024, **146**, 24670–24680.

27 W. C. Qiao, H. Qiao, X. L. Wang, H. Xu, F. Xu, Z. Sun, H. Gao and Y. F. Yao, *Small*, 2024, **20**, 2310529.

28 M. S. Lassoued, T. Wang, A. Faizan, Q.-W. Li, W.-P. Chen and Y.-Z. Zheng, *J. Mater. Chem. C*, 2022, **10**, 12574–12581.

29 Bruker Nano, Inc., Madison, WI, USA, 2019–2024.

30 L. Krause, R. Herbst-Irmer, G. M. Sheldrick and D. Stalke, *Appl. Crystallogr.*, 2015, **48**, 3–10.

31 G. M. Sheldrick, *Acta Crystallogr., Sect. A: Found. Adv.*, 2015, **71**, 3–8.

32 G. M. Sheldrick, *Acta Crystallogr., Sect. C: Struct. Chem.*, 2015, **71**, 3–8.

33 O. V. Dolomanov, L. J. Bourhis, R. J. Gildea, J. A. Howard and H. Puschmann, *J. Appl. Crystallogr.*, 2009, **42**, 339–341.

34 *SAINT V8.41*, Bruker AXS, Madison, WI, 2024.

35 J. P. Perdew, K. Burke and M. Ernzerhof, *Phys. Rev. Lett.*, 1996, **77**, 3865.

36 G. Kresse and J. Furthmüller, *Phys. Rev. B: Condens. Matter Mater. Phys.*, 1996, **54**, 11169.

37 G. Kresse and J. Furthmüller, *Comput. Mater. Sci.*, 1996, **6**, 15–50.

38 S. P. Ong, W. D. Richards, A. Jain, G. Hautier, M. Kocher, S. Cholia, D. Gunter, V. L. Chevrier, K. A. Persson and G. Ceder, *Comput. Mater. Sci.*, 2013, **68**, 314–319.

39 A. Mandal, S. Gupta, S. Dutta, S. K. Pati and S. Bhattacharyya, *Chem. Sci.*, 2023, **14**, 9770–9779.

40 L. Gao, X. Li, B. Traore, Y. Zhang, J. Fang, Y. Han, J. Even, C. Katan, K. Zhao and S. Liu, *J. Am. Chem. Soc.*, 2021, **143**, 12063–12073.

41 Q. Fan, H. Xu, S. You, Y. Ma, Y. Liu, W. Guo, X. Hu, B. Wang, C. Gao and W. Liu, *Small*, 2023, **19**, 2301594.

42 H. Yu, Z. Wei, Y. Hao, Z. Liang, Z. Fu and H. Cai, *New J. Chem.*, 2017, **41**, 9586–9589.

43 S. Maheshwari, M. B. Fridriksson, S. Seal, J. r. Meyer and F. C. Grozema, *J. Phys. Chem. C*, 2019, **123**, 14652–14661.

44 R. Roccanova, W. Ming, V. R. Whiteside, M. A. McGuire, I. R. Sellers, M.-H. Du and B. Saparov, *Inorg. Chem.*, 2017, **56**, 13878–13888.

45 C.-Y. Su, H.-G. Yi, H.-F. Ni, G.-W. Du, S.-Q. Xia, Z. Liu, Z.-X. Zhang and D.-W. Fu, *Chem. Sci.*, 2025, **16**, 23385–23393.

46 G. Chapuis, R. Kind and H. Arend, *Phys. Status Solidi A*, 1976, **36**, 285–295.

47 D. A. Popy, L. M. Loftus, J. Jiang, J. D. Einkauf, S. Kapoor, M. A. McGuire, R. Pachter and B. Saparov, *Small*, 2025, **21**, e06916.

48 H. Shoukat, T. Pinky, M. S. Muhammad, Z. Masood, A. Akbar, N. Yamamoto, S. Puri, D. N. McIlroy, B. Wang and J. Brgoch, *Inorg. Chem.*, 2025, **65**, 403–415.

49 W. Guo, H. Xu, Q. Fan, P. Zhu, Y. Ma, Y. Liu, X. Zeng, J. Luo and Z. Sun, *Adv. Opt. Mater.*, 2024, **12**, 2303291.

50 R. H. Bube, *J. Appl. Phys.*, 1962, **33**, 1733–1737.

51 A. Balcioglu, R. Ahrenkiel and F. Hasoon, *J. Appl. Phys.*, 2000, **88**, 7175–7178.

52 X. Liu, H. Zhang, B. Zhang, J. Dong, W. Jie and Y. Xu, *J. Phys. Chem. C*, 2018, **122**, 14355–14361.

53 P. Jin, Y. Tang, D. Li, Y. Wang, P. Ran, C. Zhou, Y. Yuan, W. Zhu, T. Liu and K. Liang, *Nat. Commun.*, 2023, **14**, 626.

54 Y. Zhang, Y. Liu, Z. Xu, H. Ye, Z. Yang, J. You, M. Liu, Y. He, M. G. Kanatzidis and S. Liu, *Nat. Commun.*, 2020, **11**, 2304.

55 P. Liu, Y. Xiao, Z. Yang, S. Yu and X. Meng, *Opt. Mater.*, 2022, **133**, 112972.

56 Y. Chai, Z. Juan, Y. Wu, Y. Liu and X. Li, *ACS Appl. Electron. Mater.*, 2023, **5**, 544–551.

57 P. Wang, H. Wang, J. Fu, H. Dong, W. Zhang, Z. Gao and Y. Shao, *ACS Photonics*, 2024, **11**, 5409–5417.

58 Z. Zhu, B. Zhao, R. He, H. Chen, S. Gao, Y. He and Y. Li, *ACS Appl. Mater. Interfaces*, 2024, **16**, 38799–38809.

59 (*a*) CCDC 2532216: Experimental Crystal Structure Determination, 2026, DOI: 10.5517/ccdc.csd.cc2qzzd3; (*b*) CCDC 2532217: Experimental Crystal Structure Determination, 2026, DOI: 10.5517/ccdc.csd.cc2qzzf4.